2026 IEEE International Conference on Robotics and Automation (ICRA 2026)
June 1-5, 2026. Vienna, Austria

# Wind-Aware Aerial Deployment and Control Strategy for Precision Landing of Single-Actuator Autorotating Wing

Shane Kyi Hla Win, Luke Soe Thura Win, Danial Sufiyan, Shaohui Foong

***Abstract*— The Samara Autorotating Wing (SAW) is a bio-inspired autorotating glider capable of both controlled autorotation and diving modes. This work presents control and deployment strategies that enable precision landing of the platform from low altitude. The proposed control approach leverages cyclic control and a dive maneuver to improve landing accuracy. The deployment strategy is developed by updating parameters in a simulated model to reflect real-world performance under varying wind conditions, and then using the model to predict feasible release regions for specified wind direction, speed, and altitude. A total of 56 deployments were conducted from 60 m altitude in both low-wind ($< 5$ ms$^{-1}$) and high-wind ($> 5$ ms$^{-1}$) conditions representative of the local climate. The platform achieved landings within 10 m of the target in 89% of low-wind trials and 57% of high-wind trials. These results highlight the potential of SAW platform for applications requiring high-precision remote sensor deployment.**

## I. INTRODUCTION

In recent years, remote sensor deployment has become increasingly important in applications such as wildfire detection [1][2], wildlife monitoring [3][4], and search and rescue operations [5][6]. Wireless sensor networks [7] provide critical real-time information for decision-making. Conventionally, these sensors are manually deployed [8], which can be labor-intensive and limit access to remote or hazardous areas. Consequently, there has been a growing interest in using Unmanned Aerial Vehicles (UAVs) for sensor deployment [9]–[11]. Despite progress, achieving large-scale, high-precision deployment within short time frames remains challenging.

Recent research has explored innovative approaches such as biodegradable gliders [12], luminescent seed-like fliers for physical sensing [13], and wind-dispersed microfliers [14]–[16]. While these methods demonstrate creativity in sensor deployment, they generally lack the elements required for guidance, control, and precision landing. To address this gap, several guided sensor platforms have been proposed. One example is CICADA [17], a sensor-embedded glider that can be released from UAVs or manned aircraft. Another example is the Samara Autorotating Wing (SAW) [18][19], a bio-inspired platform with a single actuator that controls its glide path (Fig. 1). A distinguishing feature of SAW is its ability to descend vertically and land softly. In addition, the platform uses only one actuator for directional control and is capable of diving maneuvers that enable rapid altitude reduction.

The design of SAW has been optimized to achieve favorable glide performance, and its transition between autorotation and diving has been studied previously [19]. Owing to its low wing loading and lightweight structure, SAW is highly sensitive to environmental wind, which can induce substantial lateral drift and degrade landing accuracy. However, when wind speed and direction are known at deployment time, this sensitivity can be exploited to predict feasible release regions that lead to precise landings. A similar principle has been demonstrated in guided parafoil systems, where ground wind measurements are incorporated to improve landing accuracy [20]. Building on this insight, the present work introduces control and deployment strategies for an updated version of SAW (mk3) to enable precision landing from low altitude under known wind conditions.

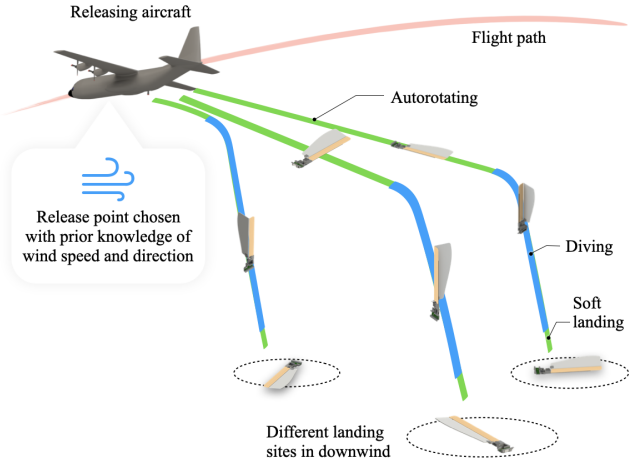


Fig. 1. With prior knowledge of wind conditions, SAW can be released from advantageous regions identified during mission planning. The combination of cyclic control and a dive mode enables high-precision landing.

The main contributions are as follows:

- A control strategy that employs pure pursuit for cyclic control and incorporates intelligent switching to dive mode to improve landing accuracy.
- A deployment strategy based on an updated simulation model that reflects real-world performance under varying wind conditions, enabling prediction of feasible release regions for specified wind direction, speed, and altitude.
- Experimental validation through 56 low-altitude deployments, demonstrating landing accuracy within 10 m of the target in 89% of trials under low-wind conditions and 57% of trials under high-wind conditions.

The authors are with Temasek Laboratories @ SUTD, Singapore University of Technology and Design (SUTD), 8 Somapah Road, Singapore 487372. Corresponding author e-mail: *foongshaohui@sutd.edu.sg*

## II. MODELING AND CONTROL STRATEGY

### A. Dynamic Model

The dynamic model of SAW, originally formulated using Blade Element Theory (BET) to compute aerodynamic forces in six degrees of freedom [19], is extended here to account for environmental wind and disturbances. Wind is modeled as a drag force $\boldsymbol{D_B}$ acting on the fuselage, expressed as

$$\boldsymbol{D_B} = C_B \boldsymbol{v_w}, \tag{1}$$

where $\boldsymbol{v_w}$ is the wind velocity and $C_B$ is a coefficient to be determined. To represent wind interaction with the wing, $C_W \boldsymbol{v_w}$ is resolved into each blade element's frame and added directly to the inflow velocity used for lift and drag computations. The lift and drag coefficients are also scaled by gains $K_L$ and $K_D$, respectively, to account for wind effects.

Since BET alone may not fully capture the dynamics, additional restoring torques $\boldsymbol{R_x}$ and $\boldsymbol{R_y}$ along the $\boldsymbol{x}$ and $\boldsymbol{y}$ axes, respectively, are introduced as

$$\boldsymbol{R_x} = C_{Tx} \boldsymbol{\omega_x}, \tag{2}$$

$$\boldsymbol{R_y} = C_{Ty} \boldsymbol{\omega_y}, \tag{3}$$

where $C_{Tx}$ and $C_{Ty}$ are coefficients to be determined, and $\boldsymbol{\omega_x}$ and $\boldsymbol{\omega_y}$ are angular velocities in the body frame. The updated free-body diagram is shown in Fig. 2.

### B. Control Strategy

Lateral motion is achieved through square cyclic control of the flap, as described in [19]. The flap oscillates during each rotation cycle, increasing and decreasing lift relative to a commanded azimuth direction. In the present strategy, pure pursuit control is used to define the desired azimuth direction $\lambda_t$, while the flap amplitude $\gamma_{amp}$ is maintained at a constant value.

Due to its low wing loading, similar to that of a natural samara seed, SAW is highly sensitive to wind and turbulence, resulting in substantial drift under windy conditions. To mitigate this effect, a control strategy that exploits the dive mode is introduced (Fig. 3). Dive mode is activated when the platform is within $r_c$ of the target, causing it to descend rapidly and reducing wind influence during the final approach. The dive mode is deactivated when the altitude falls below $h_c$, after which the system transitions to autorotation and flares for a soft landing near the target.

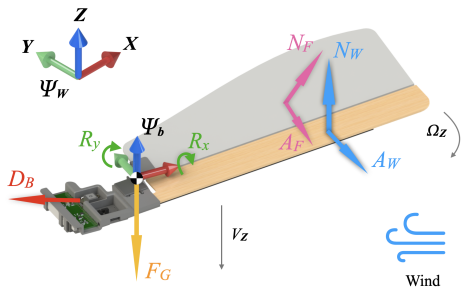


Fig. 2. Dynamic model of SAW updated to include environmental wind effects and restoring torques.

The transition between autorotation and dive mode, previously characterized in [19], is triggered by deflecting the flap to a fixed angle $\gamma_{dive}$. This stalls the wing, causing an abrupt loss of lift and initiating a rapid, near-vertical descent. Recovery is achieved by returning the flap to neutral, which restores lift and resumes autorotation in the intended rotation direction. The transition in both directions occurs within approximately one second. During dive mode, active control is not applied, and the platform descends with increasing vertical velocity. Horizontal velocity is expected to decrease due to the reduction in lift and increased aerodynamic drag, although some lateral drift may still occur under wind influence. Because the dive duration is brief in this work due to low altitude deployment, the platform may retain a significant portion of its pre-dive horizontal velocity. Accordingly, the distance threshold $r_c$ is selected differently for low- and high-wind conditions to account for this effect.

The on-board GPS receiver provides position updates in latitude $\Phi_r$ and longitude $\Lambda_r$. The platform's pitch forward ($+\theta_d$) aligns with the North direction, while roll right ($+\phi_d$) aligns with the East direction. The target direction $\lambda_t$ is computed as

$$\theta_d = C_\Phi \left(\Phi_0 - \Phi_r\right), \tag{4}$$

$$\phi_d = C_\Lambda \left(\Lambda_0 - \Lambda_r\right), \tag{5}$$

$$\lambda_t = \arctan\left(\frac{\theta_d}{\phi_d}\right), \tag{6}$$

where $\Phi_0$ and $\Lambda_0$ are the target latitude and longitude, and $C_\Phi$ and $C_\Lambda$ are conversion factors for latitude and longitude, respectively, given by

$$C_\Phi = \frac{a(1-e^2)}{(1-e^2\sin^2\Phi_0)^{3/2}}, \tag{7}$$

$$C_\Lambda = \frac{a\cos\Phi_0}{\sqrt{1-e^2\sin^2\Phi_0}}, \tag{8}$$

with $a = 6\,378\,137.0$ m as the Earth's semi-major axis and $e = 0.0818191909289$ as its eccentricity. The distance to target $d_t$ is then computed as

$$d_t = \sqrt{\theta_d^2 + \phi_d^2}. \tag{9}$$

Dive mode is activated when $d_t < r_c$, and deactivated when $h < h_c$, where $h$ is the altitude above ground.

## III. DEPLOYMENT STRATEGY

The deployment strategy is critical for achieving precise landings, as the trajectory of SAW is highly sensitive to real-time environmental wind conditions.

An algorithm is developed to determine the release region for a given wind speed, direction, and release altitude. Using a simulated model correlated with data from real-life deployments, potential trajectories under various wind conditions can be determined. By applying these trajectories inversely, the corresponding release regions are identified.

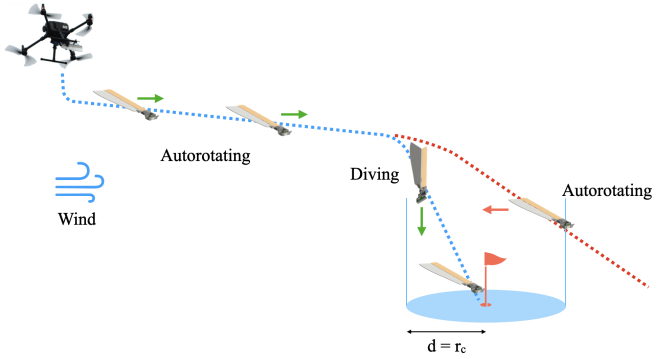


Fig. 3. Control strategy incorporating dive mode to improve landing accuracy.

### A. Simulated Model

The performance of SAW in real-life wind conditions was recorded to correlate with simulation. A new variant of SAW (mk3), described in Section IV-A, was used to collect performance data. A total of 16 drops were performed, with each drop consisting of two simultaneous releases: one in *passive mode*, allowing wind to determine the trajectory, and the other in *active mode*, where cyclic control directed flight toward fixed headings. The average wind speed during these tests was 1.42 $\mathrm{m\,s^{-1}}$ (standard deviation 0.69 $\mathrm{m\,s^{-1}}$), with a minimum of 0.6 $\mathrm{m\,s^{-1}}$ and maximum of 2.6 $\mathrm{m\,s^{-1}}$.

The simulated model was updated to match the observed performance. Specifically, the parameters $\mathbf{\Gamma} = [C_{Tx}, C_{Ty}, C_B, C_W, K_L, K_D]$ shown in Table I were tuned.

TABLE I

PARAMETERS SELECTED FOR FINE-TUNING OF THE SIMULATED MODEL

| Parameter | Symbol |
|---|---|
| Restoring torque coefficient (X-axis) | $C_{Tx}$ |
| Restoring torque coefficient (Y-axis) | $C_{Ty}$ |
| Body wind drag coefficient | $C_B$ |
| Wing wind drag coefficient | $C_W$ |
| Lift coefficient gain | $K_L$ |
| Drag coefficient gain | $K_D$ |

The suitable values of $\mathbf{\Gamma}$ were obtained by minimizing the error between simulated and real trajectories. The error was computed as the sum of squared differences between the simulated and observed landing points:

$$\min_{\mathbf{\Gamma}} \sum_{i=1}^{16} \left( (x_{\text{sim},i} - x_{\text{real},i})^2 + (y_{\text{sim},i} - y_{\text{real},i})^2 \right) \tag{10}$$

where all 16 real passive-mode trajectories were compared against simulation. The optimization was carried out using Genetic Algorithm in MATLAB.

### B. Results

Figure 4 shows the trajectories of the tuned simulation model compared with real-life data. Trajectories with the same ID correspond to the same release instance, where one unit flew passively and the other actively. The simulated

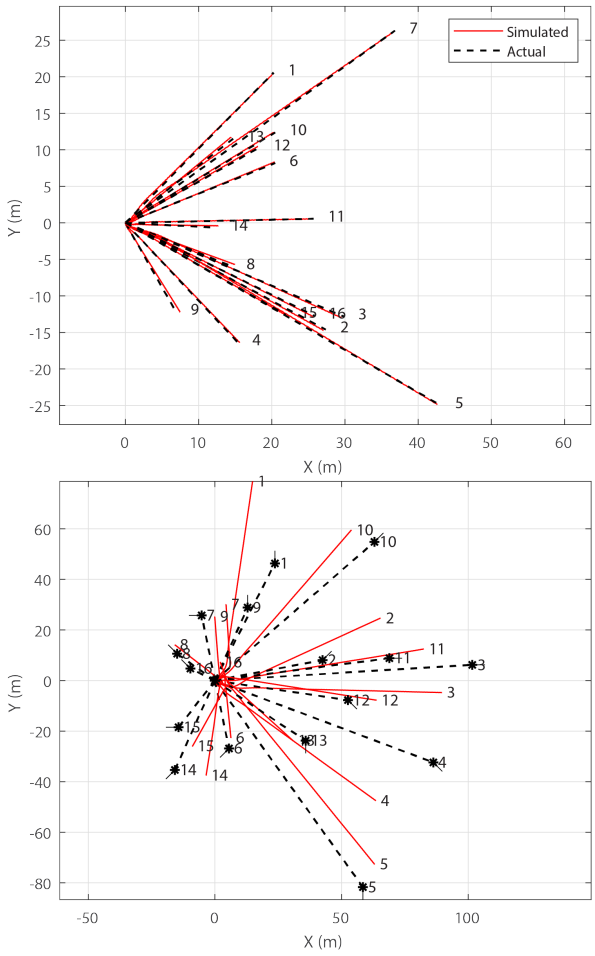


Fig. 4. Top: Trajectories of SAW in passive mode for real and simulated models. Bottom: Trajectories of SAW in active mode for real and simulated models. Each drop ID corresponds to the same release instance. The tail line in the bottom plot represents the desired azimuth direction $\lambda_t$ applied throughout flight.

trajectories closely match the observed data. The RMSE between simulation and experiment was 0.36 m for passive flight and 16.22 m for active flight.

The tuned model was then used to predict SAW trajectories under varying wind conditions. Simulations were performed for fixed cyclic inputs in 16 directions (full 360° in 22.5° increments) at wind speeds $v \in [0, 6]$ $\mathrm{m\,s^{-1}}$, in steps of 1 $\mathrm{m\,s^{-1}}$. The wind direction was fixed eastward.

From these simulations, glide ratio data $g_{xi}(v)$ and $g_{yi}(v)$ were extracted for $i \in [1, 16]$, where glide ratio is defined as

$$g = \frac{\text{distance}}{\text{height}}. \tag{11}$$

Here, $g_{xi}$ and $g_{yi}$ denote the horizontal displacement per unit altitude loss in the East and North directions, respectively.

To generalize glide ratios for non-integer wind speeds, polynomial regression was performed on $g_{xi}(v)$ and $g_{yi}(v)$ using a third-order polynomial:

$$g_{xi}(v) = \sum_{j=0}^{3} a_{xj} v^j, \tag{12}$$

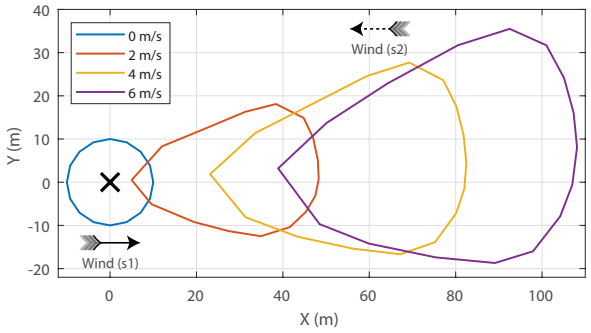


Fig. 5. Scenario 1 (s1): SAW is released from (0,0) at 60 m altitude with eastward wind. Landing regions are shown for different wind speeds. Scenario 2 (s2): By inverse logic, the same shapes represent potential release regions for target landing at (0,0) when wind direction is inverted (westward).

$$g_{yi}(v) = \sum_{j=0}^{3} a_{yj} v^j, \tag{13}$$

where $a_{xj}$ and $a_{yj}$ are polynomial coefficients.

For a given release altitude $h_r$, the final landing point can be estimated as

$$x_{fi} = x_0 + h_r g_{xi}(v), \tag{14}$$

$$y_{fi} = y_0 + h_r g_{yi}(v), \tag{15}$$

where $(x_0, y_0)$ is the release point and $(x_{fi}, y_{fi})$ is the predicted landing location under constant cyclic input $\lambda_i$.

Figure 5 illustrates the predicted landing regions for eastward winds. At zero wind speed, the landing region forms a circle, as SAW can move equally in all directions. With increasing wind speed, the region elongates along the wind direction, highlighting the wind's influence. The shape also skews northward, attributed to dissymmetry of lift in the rotor plane and SAW's clockwise rotation.

Applying inverse logic, these landing regions can also represent potential release zones for precise targeting. For example, if SAW is intended to land at $(0, 0)$ under westward wind, release should occur from within the predicted regions in Fig. 5 (scenario 2). This approach can be generalized to any wind direction by rotating the predicted region accordingly.

## IV. Experiment

### A. Experiment Setup

The SAW mk3 prototype developed for this study is shown in Fig. 6. It features a printed circuit board (PCB) body that houses the electronics and battery. The microcontroller is a Teensy 4.1, connected to a magnetometer (MMC5983MA), an RC receiver (TBS Crossfire Nano RX), a GPS module (Sparkfun XA1110), and a servo (Spektrum H3065). The wing is reinforced by gluing a thin carbon fiber sheet to balsa wood (leading edge) and foam (flap). Other support structures are 3D printed using Markforged Onyx material. The total weight of the SAW mk3 prototype is 80 g.

SAW units were deployed using a DJI Matrice 300 UAV (Fig. 7). The UAV was equipped with a Trisonica Mini wind

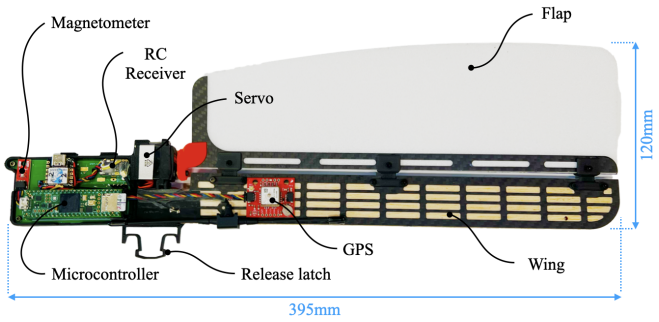


Fig. 6. SAW mk3 prototype used in experiments.

sensor mounted approximately 0.6 m above the propeller plane, where airflow interference was negligible. The sensor measured two-dimensional wind speed and direction. A Teensy 4.1 microcontroller logged wind and GPS (Sparkfun XA1110) data locally on an SD card and transmitted telemetry via a LoRa transceiver (Reyax RYLR998).

The UAV is equipped with a custom payload bay capable of carrying up to three SAW units, which could be released individually. The payload bay is mounted directly beneath the UAV, simplifying both the bay's design and the UAV's flight dynamics. The propeller downwash has minimal influence on the SAW's trajectory, as each unit typically requires approximately 1.5 s or 5.4 m of descent to reach a stable autorotation state, beyond which downwash effects are negligible. In strong winds, SAW may transition into autorotation immediately upon release, but its rapid lateral drift quickly carries it outside the downwash region.

Flights were conducted manually by a pilot, with SAWs released once the desired conditions were met. A ground control station (GCS) displayed real-time predictions of the release region based on measured wind and altitude data.

To assess vertical wind variation, the UAV ascended in 10 m increments, hovering for 100 s at each altitude from 10 m to 60 m above ground level. Figure 8 shows the resulting probability density estimates of wind speed and direction. Wind conditions were generally consistent across altitudes, except near 10 m where wind speed was lower due


Fig. 7. Deployment UAV used in trials, equipped with wind sensor and payload bay.

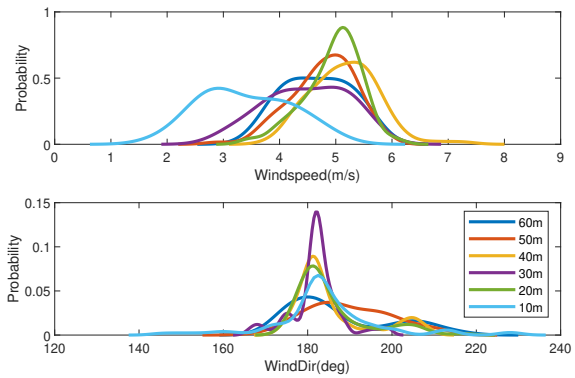


Fig. 8. Probability density estimates of wind speed and direction from 10 m to 60 m altitude.

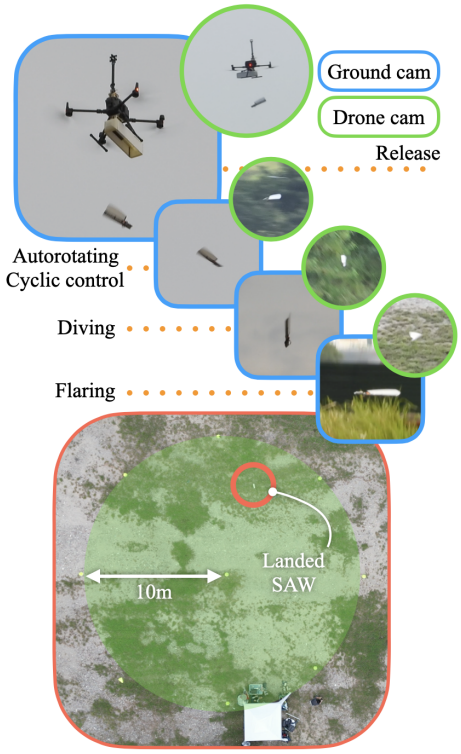


Fig. 9. Deployment of SAW from UAV as seen from ground and drone cameras.

to boundary layer effects.

Figure 9 shows a representative deployment sequence as captured by both ground and onboard UAV cameras.

### B. Results

A total of 56 deployments were conducted from an altitude of 60 m. Half were performed under relatively calm conditions ($< 5$ m s$^{-1}$ average wind speed) and half under windier conditions ($> 5$ m s$^{-1}$). Dive mode was triggered automatically when the target distance threshold was reached ($r_c = 10$ m for low-wind and $r_c = 40$ m for high-wind conditions). Dive mode was deactivated manually when the altitude fell below 20 m.

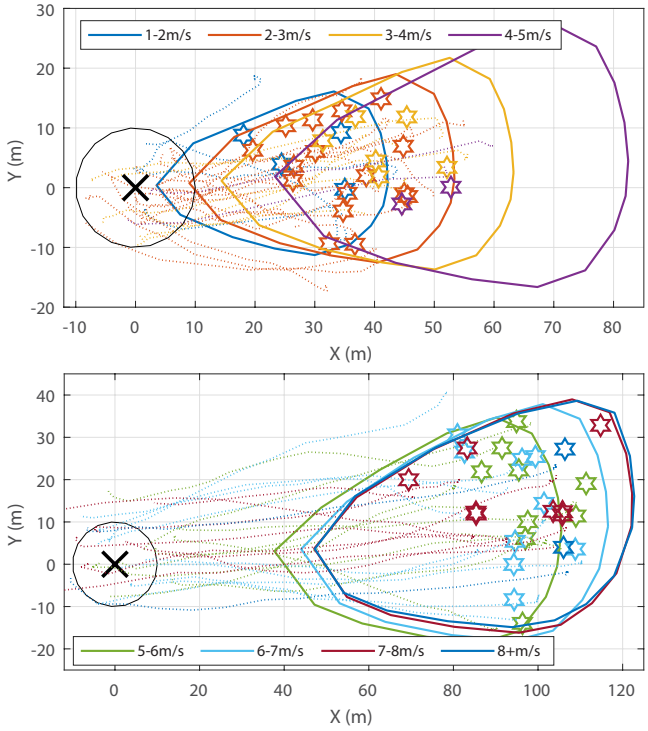


Fig. 10. Top: Deployment results under low wind conditions. Bottom: Deployment results under high wind conditions. Hexagrams: release points; dotted lines: trajectories; 'x': target location; black circle: 10 m target radius. Color coding links release region, release point, and trajectory within the same wind-speed bracket.

Figure 10 shows the predicted release regions, actual UAV release points, and resulting trajectories. Wind direction is normalized to a common Westward axis for comparison. In some cases, trajectory origins appear offset from release points due to degraded GPS reception inside the payload bay. The release location, however, was accurately determined using the UAV's GPS data. After release, the on-board GPS receiver rapidly regained accuracy due to hot starts, achieving position fixes within approximately 1 s and typical horizontal accuracies better than 3 m. Deployments from predicted release regions consistently yielded high landing precision. As expected, stronger winds increased the allowable release distance, with some high-wind deployments released nearly 120 m upwind of the target.

Figure 11 shows two representative examples: one under calm conditions with the UAV positioned near the center of the predicted region, and one under stronger winds with the UAV at the region's edge. In both cases, SAW landed within 10 m of the target, confirming robustness of the release-region approach.

Table II summarizes overall performance. SAW achieved landing within 10 m of the target in 89% of calm-condition trials and 57% of windy-condition trials. The average distance from the target increased with wind speed, as shown in Fig. 12, particularly above 5 m s$^{-1}$. Occasional deviations greater than 20 m were observed, likely due to sudden wind shifts or degraded GPS accuracy.

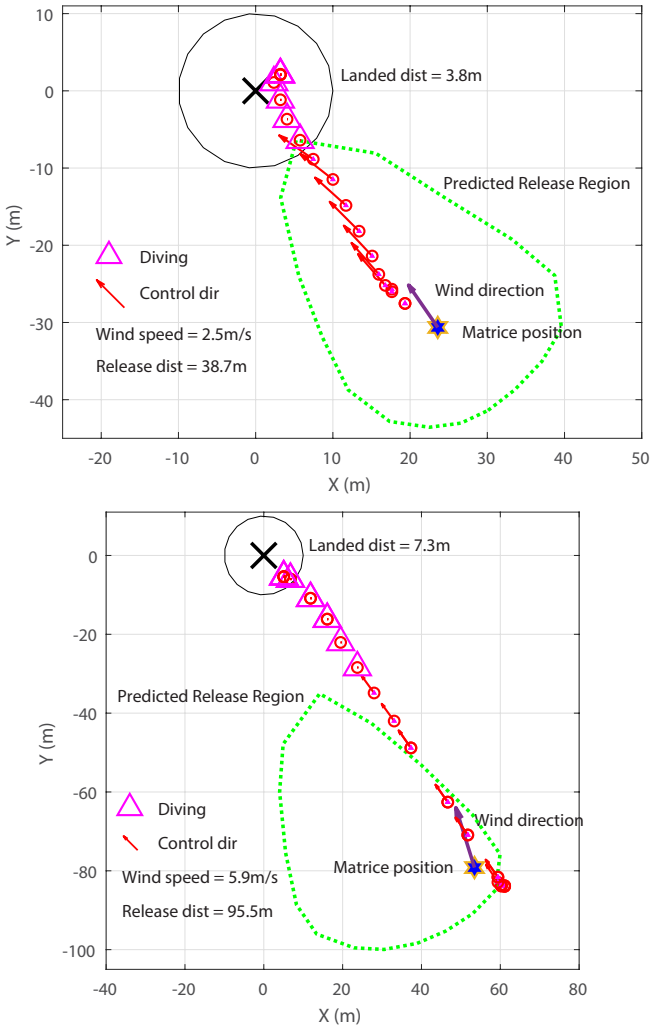


Fig. 11. Representative deployments: Top, low-wind scenario with UAV near center of release region; Bottom, high-wind scenario with UAV at release region edge. Red arrows indicate applied cyclic control and controlled direction $\lambda_t$; purple triangle indicates dive mode activation.

## V. CONCLUSIONS AND FUTURE WORK

This paper presented control and deployment strategies for the precision landing of the Samara Autorotating Wing (SAW) platform. The proposed approach combines pure pursuit–based cyclic control with an active dive mode to improve landing accuracy under windy conditions. The deployment strategy leverages a simulation model correlated with real-world data to identify potential release regions. Field trials showed that SAW could land within 10 m of the target in 89% of cases under low-wind conditions and 57% under high-wind conditions.

Future work will focus on advancing the control architecture. Beyond pure pursuit, approaches such as Model Predictive Control or Reinforcement Learning could enhance robustness to dynamic conditions, including varying wind profiles with altitude. Hardware improvements, such as higher-precision GPS and barometric sensors, could further refine autonomous diving and recovery. In addition, integrating onboard real-time wind estimation will allow adaptive control during descent. On the deployment side, extending the simulation framework to incorporate more complex wind models and terrain effects could improve release planning.

Ultimately, these developments aim to extend SAW's operational envelope to higher altitudes and more challenging environments. With its lightweight, low-cost, and energy-efficient design, SAW shows promise as a versatile platform for remote sensor deployment across diverse applications, including search and rescue, wildfire and wildlife monitoring, and even enabling the recovery of upper-atmospheric weather sondes.

TABLE II

SUMMARY OF REAL-LIFE DEPLOYMENT RESULTS

| | **Low wind** | **High wind** |
|---|---|---|
| Accuracy within 10 m | 89% | 57% |
| Total attempts | 28 | 28 |
| Average distance from target | 6.2 m | 10.3 m |
| Average wind speed | 2.7 $ms^{-1}$ | 6.6 $ms^{-1}$ |
| Average release distance | 36.5 m | 98.4 m |

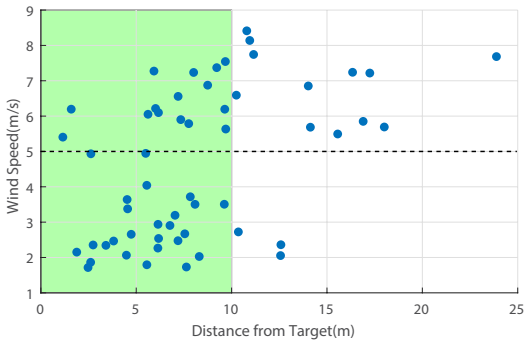


Fig. 12. Scatter plot of landing distance from target vs. wind speed.

## ACKNOWLEDGMENT

This project is supported by Temasek Laboratories @ SUTD and the Ministry of Education, Singapore (T2EP50123-0017/MOE-T2EP50123-0004). The authors would like to thank Mr Brian Leonard Suhadi for his assistance in conducting the field experiments.

## REFERENCES

[1] D. M. Doolin and N. Sitar, "Wireless sensors for wildfire monitoring," in *Smart structures and materials 2005: sensors and smart structures technologies for civil, mechanical, and aerospace systems*, SPIE, vol. 5765, 2005, pp. 477–484.

[2] A. Somov, "Wildfire safety with wireless sensor networks," *EAI Endorsed Transactions on Ambient Systems*, vol. 1, no. 1, 2011.

[3] V. Dyo, S. A. Ellwood, D. W. Macdonald, *et al.*, "Wildsensing: Design and deployment of a sustainable sensor network for wildlife monitoring," *ACM Transactions on Sensor Networks (TOSN)*, vol. 8, no. 4, pp. 1–33, 2012.

[4] J. P. Dominguez-Morales, A. Rios-Navarro, M. Dominguez-Morales, *et al.*, "Wireless sensor network for wildlife tracking and behavior classification of animals in doñana," *IEEE Communications Letters*, vol. 20, no. 12, pp. 2534–2537, 2016.

[5] J. Bravo-Arrabal, P. Zambrana, J. J. Fernández-Lozano, J. A. Gómez-Ruiz, J. S. Barba, and A. García-Cerezo, "Realistic deployment of hybrid wireless sensor networks based on zigbee and lora for search and rescue applications," *IEEE Access*, vol. 10, pp. 64 618–64 637, 2022.

[6] J. Reich and E. Sklar, "Robot-sensor networks for search and rescue," in *IEEE International Workshop on Safety, Security and Rescue Robotics*, vol. 22, 2006.

[7] S. Abdollahzadeh and N. J. Navimipour, "Deployment strategies in the wireless sensor network: A comprehensive review," *Computer Communications*, vol. 91, pp. 1–16, 2016.

[8] R. Stoleru, T. He, and J. A. Stankovic, "Walking gps: A practical solution for localization in manually deployed wireless sensor networks," in *29th annual IEEE international conference on local computer networks*, IEEE, 2004, pp. 480–489.

[9] V. Iyer, M. Kim, S. Xue, A. Wang, and S. Gollakota, "Airdropping sensor networks from drones and insects," in *Proceedings of the 26th Annual International Conference on Mobile Computing and Networking*, 2020, pp. 1–14.

[10] K. Sugiura, "Sumo-ss: Submodular optimization sensor scattering for deploying sensor networks by drones," *IEEE Robotics and Automation Letters*, vol. 3, no. 4, pp. 2963–2970, 2018.

[11] L. Y. Sørensen, L. T. Jacobsen, and J. P. Hansen, "Low cost and flexible uav deployment of sensors," *Sensors*, vol. 17, no. 1, p. 154, 2017.

[12] L. Girardi, R. Wu, Y. Fukatsu, H. Shigemune, and S. Mintchev, "Biodegradable gliding paper flyers fabricated through inkjet printing," in *2024 IEEE/RSJ International Conference on Intelligent Robots and Systems (IROS)*, 2024, pp. 10 334–10 341. DOI: 10.1109/IROS58592.2024.10801580.

[13] K. Cikalleshi, A. Nexha, T. Kister, *et al.*, "A printed luminescent flier inspired by plant seeds for eco-friendly physical sensing," *Science Advances*, vol. 9, no. 46, eadi8492, 2023.

[14] B. H. Kim, K. Li, J.-T. Kim, *et al.*, "Three-dimensional electronic microfliers inspired by wind-dispersed seeds," *Nature*, vol. 597, no. 7877, pp. 503–510, 2021.

[15] K. Johnson, V. Arroyos, A. Ferran, *et al.*, "Solar-powered shape-changing origami microfliers," *Science Robotics*, vol. 8, no. 82, eadg4276, 2023.

[16] V. Iyer, H. Gaensbauer, T. L. Daniel, and S. Gollakota, "Wind dispersal of battery-free wireless devices," *Nature*, vol. 603, no. 7901, pp. 427–433, 2022.

[17] A. D. Kahn and D. J. Edwards, "Navigation, guidance, and control of a micro unmanned aerial glider," *Journal of Guidance, Control, and Dynamics*, pp. 1–11, 2019.

[18] S. K. H. Win, L. S. T. Win, D. Sufiyan, G. S. Soh, and S. Foong, "Dynamics and control of a collaborative and separating descent of samara autorotating wings," *IEEE Robotics and Automation Letters*, vol. 4, no. 3, pp. 3067–3074, 2019.

[19] S. K. H. Win, L. S. T. Win, D. Sufiyan, G. S. Soh, and S. Foong, "An agile samara-inspired single-actuator aerial robot capable of autorotation and diving," *IEEE Transactions on Robotics*, vol. 38, no. 2, pp. 1033–1046, 2021.

[20] M. R. Cacan, E. Scheuermann, M. Ward, M. Costello, and N. Slegers, "Autonomous airdrop systems employing ground wind measurements for improved landing accuracy," *IEEE/ASME Transactions on Mechatronics*, vol. 20, no. 6, pp. 3060–3070, 2015.